

We are IntechOpen, the world's leading publisher of Open Access books Built by scientists, for scientists

6,900

Open access books available

186,000

International authors and editors

200M

Downloads

Our authors are among the

154

Countries delivered to

TOP 1%

most cited scientists

12.2%

Contributors from top 500 universities



WEB OF SCIENCE™

Selection of our books indexed in the Book Citation Index
in Web of Science™ Core Collection (BKCI)

Interested in publishing with us?
Contact book.department@intechopen.com

Numbers displayed above are based on latest data collected.
For more information visit www.intechopen.com



Cathodoluminescence of Surface Plasmon Induced Light Emission

Naoki Yamamoto

*Physics Department, Tokyo Institute of Technology, Tokyo,
Japan*

1. Introduction

Cathodoluminescence (CL) is light emitting phenomena induced by high energy electrons incident on materials. The CL is sometimes defined as light emission caused by the inner electronic transition between the electronic states or bands associated with excitation by the incident electron beam. The typical one is the radiative recombination of carriers in semiconductors, such as the band to band transition (Yamamoto, 2010). CL measurement has been performed by combining a light detection system with a scanning electron microscope (SEM) or scanning transmission electron microscope (STEM), in which a focused electron beam is scanned over a specimen and simultaneously a scanning image is recorded by using an emitted light signal. This technique is called cathodoluminescence. This technique provides us the information of local electronic states from the CL spectrum, and spatial distribution of luminescence centers from the CL image, and thus has been applied to the characterization of structural defects such as dislocations and semiconductor quantum structures. On the other hand there are other types of light emission caused by a high-energy electron passing through or nearby a medium (Yamamoto et al., 1996, 2001a), such as Cherenkov radiation, transition radiation and Smith-Purcell radiation. A high-energy electron incident on a metal surface can excite a surface plasmon which propagates on a corrugated metal surface to emit light. Recently such light emission induced by surface plasmon has been intensively studied by the CL technique.

Surface plasmon (SP) is collective oscillation of surface charge on a metal surface, and is classified into two types, localized surface plasmon (LSP) and surface plasmon polariton (SPP). The LSP is localized at a narrow space of nano-structures such as particles, and SPP is a transverse magnetic (TM) mode electromagnetic wave propagating at a metal/dielectric interface, which is evanescently confined in the perpendicular direction (Raether, 1988). SPs can produce strong electromagnetic field at a localized area and are utilized for bio-sensors (Homola, 2008) and solar cells (Catchpole and Polman, 2008). SPP can be confined into a narrow area beyond the diffraction limit of light and has a potential in optical circuits and optical computer applications. This recently developed field is called "Plasmonics" (Maier, 2007; Brongersma and Kik, 2007).

The author has intensively studied light emission from metal nano-particles and nano-structures using a light detection system combined with a scanning transmission electron microscope (STEM) (Yamamoto et al., 2001a). The use of this system has an advantage for

selectively examining a localized region using a converged electron beam with a probe size of 1 nm, and also observing emission intensity distribution as a monochromatic photon map. The emission angle can be selected by a light detection system using a parabolic mirror and a movable mask, which enables angle-resolved measurement. Mie and gap modes of LSP in spherical metal particles were investigated, and the size dependences of the resonant energies of the modes were found (Yamamoto et al., 2001b). The dispersion relation of SPP propagating on a flat surface was derived by the observation of the beam-scan spectral image across a surface step (Yamamoto and Suzuki, 2008). Dispersion patterns of SPP in 1D and 2D plasmonic crystals were obtained from the angle-resolved spectral patterns, and the SPP modes were identified from the photon maps, which mimicked standing SPP waves in a real space (Suzuki and Yamamoto, 2009; Takeuchi and Yamamoto, 2011).

2. Cathodoluminescence technique

2.1 System

Cathodoluminescence system is based on a scanning transmission electron microscope (STEM) or a transmission electron microscope (TEM) equipped with a beam scanning system, which is combined with a light detection system. It is needed to alter an ordinary setup of STEM to insert a light collection mirror inside a pole piece gap of the objective lens. Geometry of a light collection mirror and set-up of the light detection system to select polarization of light and emission direction are shown.

Pole piece

A standard high-resolution STEM equips a narrow gap pole piece for the objective lens. However, there is not enough space to insert a light collection mirror around a specimen between a specimen holder and an upper part of the pole piece. For example, the pole piece gap of JEM2000FX TEM (JEOL Co. Ltd.) for the analytical version is 15 mm and a height of the mirror is 5 mm. The use of wide gap pole piece reduces the resolution of STEM. In addition a probe size of the electron beam becomes 10 nm or larger, when a large beam current of the order of 1 nA is used to induce sufficient light intensity. However, recent development of the spherical aberration (Cs) corrector and field emission gun (FEG) drastically improve the resolution of TEM/STEM. We realized a 1 nm size probe at 1 nA beam current at 80 kV and 200kV by using FEG and Cs corrector in JEM2100F STEM.

Light collection mirror

An ellipsoidal mirror and parabolic mirror were used for light collection in STEM-CL, and the latter has an advantage in angle-resolved measurement. The parabolic mirror is set up above the sample. The parabolic curve of the mirror is expressed as

$$4p(p-x) = y^2 + z^2, \quad (1)$$

using the Cartesian coordinates as shown in Fig. 1, where the origin is taken at the focal point of the parabola. The distance p between the focal point and mirror surface along the x direction is taken to be 2 mm in our system. The parabola mirror was cut into two pieces and then each mirror is 10 mm in width and 5 mm in height. In addition the bottom of the mirror is 0.2 mm higher than the parabolic axis to make a clearance between a specimen

surface and the mirror. The mirror has a 0.6 mm hole located 4 mm ($=2p$) above the focal point, through which the electron beam illuminates the specimen. Total solid angle subtended by the mirror from the focal point is about 60% of the solid angle of hemisphere. The mirror surface is expressed by the polar coordinates as

$$\begin{cases} x = r \sin \theta \cos \varphi = 2p \frac{\sin \theta \cos \varphi}{1 + \sin \theta \cos \varphi} \\ y = r \sin \theta \sin \varphi = 2p \frac{\sin \theta \sin \varphi}{1 + \sin \theta \cos \varphi} \\ z = r \cos \theta = 2p \frac{\cos \theta}{1 + \sin \theta \cos \varphi} \end{cases} \quad (2)$$

where the radial distance r is expressed by the polar angle θ and azimuth angle φ as

$$r = \frac{2p}{1 + \sin \theta \cos \varphi}. \quad (3)$$

In particular case that $\varphi=0$ and then $y=0$, the following relation holds between θ and z ,

$$\sin \theta = \frac{4p^2 - z^2}{4p^2 + z^2} = \frac{1 - \eta^2}{1 + \eta^2}, \quad (4)$$

where we put $\eta = \frac{z}{2p}$.

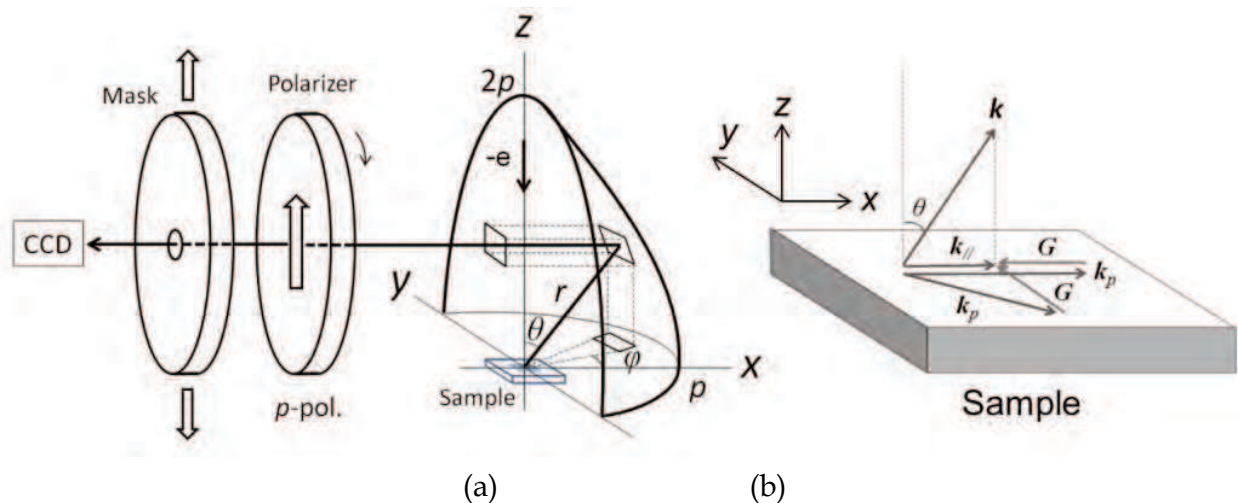


Fig. 1. (a) Geometry of a parabolic mirror and experimental set up for the angle resolved measurement. (b) Relation among the wave vectors of an emitting photon and associated SPPs.

It is needed to precisely adjust a mirror position with respect to a light emerging point on a specimen illuminated by the electron probe. The mirror is supported by a mirror holder fixed to the STEM, and the xyz positions of the mirror can be adjusted by three micrometers in the holder. The mirror can be retracted from the electron beam pass by the mirror holder.

The emitted light becomes a parallel ray after reflected by the parabolic mirror, and passes through a hollow inside the mirror holder into outside the STEM. Several parts such as an anti-contamination tip surrounding the pole piece are modified for the insertion of the mirror and mirror holder.

Light detection system

A light detection system equipped with the STEM is illustrated in Fig.2. The parallel ray from the parabolic mirror passes through a polarizer and a lens, and is switched to three paths by a flat mirror. One path leads to a photomultiplier tube for mainly photon map imaging, and another path leads to a CCD camera for imaging the parabolic mirror. The mirror position is adjusted using a luminescent specimen so as that an emission pattern in the mirror image spreads over the mirror plane observed by the CCD camera, which ensures that the parabolic mirror is focused at the light emerging point. In the straight path, the parallel ray goes through a mask with a small hole supported by an X-Y stage. The emission image on the parabolic mirror is transformed into a mask plane by the single lens. A part of the parallel ray passes through the hole, and is detected by a CCD detector to measure an angle resolved spectrum.

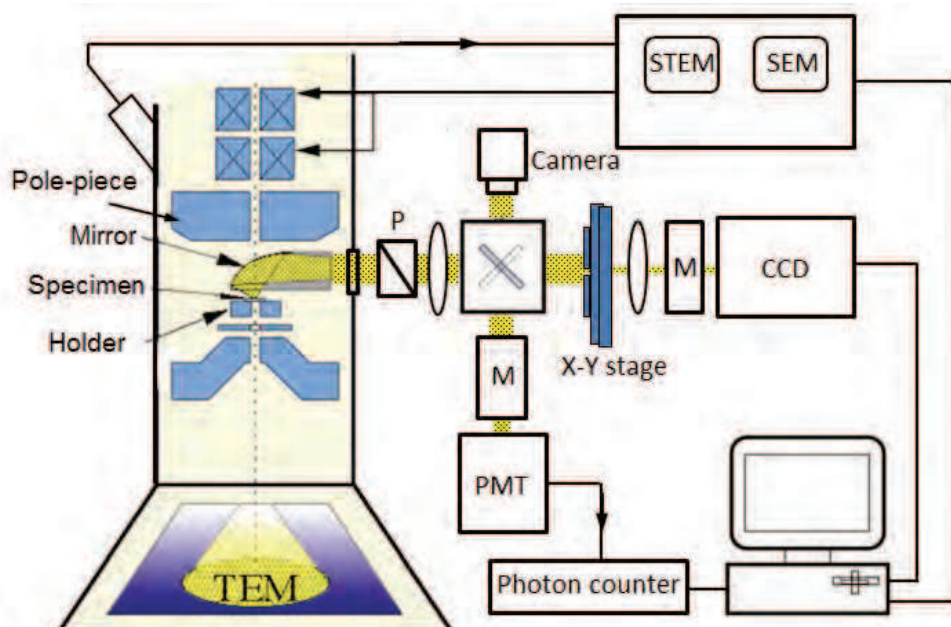


Fig. 2. Light detection system combined with a TEM/STEM

The polarization direction of light is determined by the polarizer. Here we define p -polarization as parallel to the emission plane (the x - z plane in Fig.1) subtended by the axis of parabola and normal to the specimen surface, and s -polarization is normal to the emission plane. For the angle-resolved measurement, a mask with a small hole is set on the X-Y stage. The mask position selects the emission direction of the detected light, which is specified by the angles θ and φ . The mask is moved vertically when the azimuth angle $\varphi = 0^\circ$ and the emission spectra are successively measured to determine the θ -dependence. This procedure provides an emission intensity distribution of an angle-resolved spectrum (ARS), which shows variations with angle θ and forms an ARS pattern, $I(\theta, E)$ (Suzuki, 2009).

2.2 CL measurements

Photon map

Photon map is a 2 dimensional scanning image as shown in Fig.3 (a). The electron beam is controlled by a computer through the beam scanning system of the TEM/STEM, and is scanned on a specimen surface step by step. A photon signal is successively acquired by the PMT or CCD during the duration time at each point where the electron beam is stopped. Each point corresponds to a pixel in a scanning image of a photon map. The step interval and duration time for one pixel are adjustable, and simultaneous observation of STEM image for a thin specimen and SEM image for a bulk specimen is possible. The SEM image can be observed in the SEM mode using the beam scanning system of TEM/STEM. The simultaneous observation of photon map and STEM or SEM image enables us to directly compare the emission distribution with a specimen structure.

Polarization and wavelength of the parallel ray are selected by the polarizer and monochromator, so we observe a polarized monochromatic photon map. A panchromatic photon map is sometimes useful for quick scan due to strong intensity, which is possible by setting a specular reflection in the monochromator. In the CL system shown in Fig.2, the photon map observed by the PMT uses the light intensity collected over a wide solid angle subtended by the parabolic mirror. When using the CCD detector, an emission spectrum is stored for each pixel, so monochromatic photon maps over the continuous photon energy range can be obtained by one scan measurement. However, measurement of the photon map by the CCD takes more than 10 times longer than that by the PMT.

Beam-scan spectral image

Emission spectra were successively measured by scanning the electron beam along a line in the experimental arrangement of Fig. 3(b). The lower figure in Fig. 3(b) shows a Beam-scan spectral image created by aligning the observed spectra with respect to the electron beam position, where the vertical axis indicates photon energy. When combining the angle resolved measurement to select emission angle of the detected light, a beam-scan spectral image can reveal distribution of a standing SPP wave as observed in the plasmonic crystal (Suzuki and Yamamoto, 2009; Takeuchi and Yamamoto, 2011).

Angle-resolved spectral pattern

Figure 3(c) shows the experimental arrangement for the measurement of angle-resolved spectral (ARS) pattern. The mask can be moved in a plane perpendicular to the x axis by an X-Y stage. Only a part of the parallel ray can go through a small hole in the mask, and this means that the emission direction of the detected light specified by angles θ and φ is selected by the mask. We move the mask vertically under the condition of $\varphi = 0^\circ$ and measure emission spectra successively to find the θ -dependence. Thus the direction of the detected light lies on the x - z plane, i.e., the azimuth angle $\varphi = 0^\circ$. The mixing of the polarization by the reflection at the mirror can be neglected for the light emitted in the direction parallel to the x - z plane. This measurement gives successive emission spectra which show variation with emission angle θ . ARS pattern is created by aligning the observed spectra with respect to the emission angle as in Fig. 3(c), where the vertical axis indicates photon energy. In the original data, the horizontal axis indicates the z position of the hole instead of the emission angle. The horizontal coordinate in the ARS pattern is changed from z to θ by using eq. (4), and then the ARS pattern is expressed as a function of θ and E , i.e., $I(\theta, E)$.

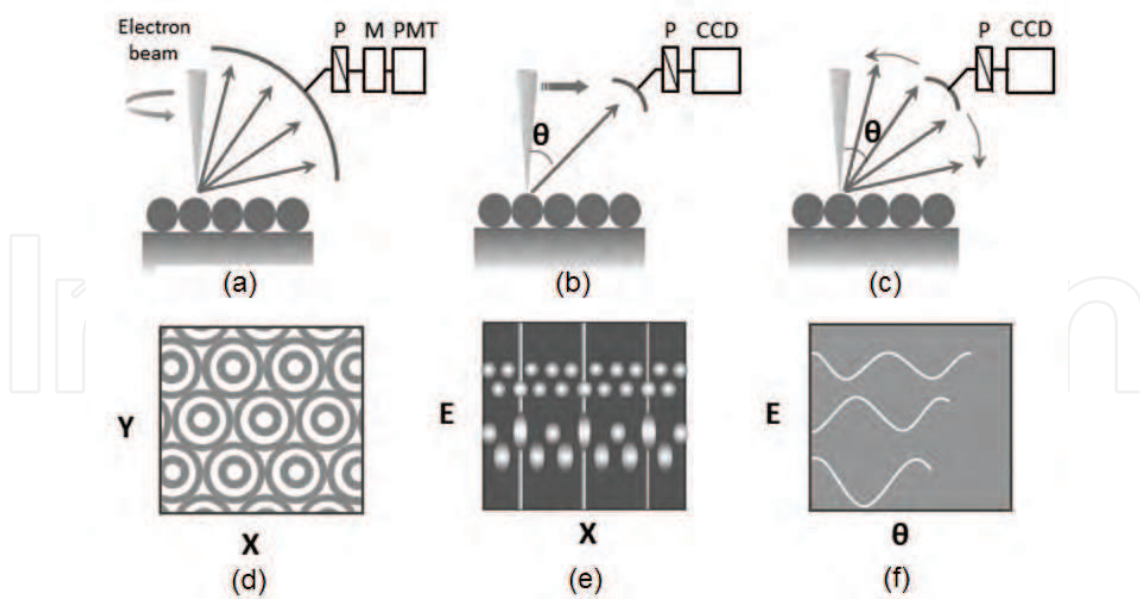


Fig. 3. Schematic diagram of experimental setup for the measurement of (a) photon map, (b) Beam-scan spectral image and (c) ARS pattern, and (d)-(f) show the observed patterns.

Dispersion pattern

The ARS pattern is transformed into the dispersion pattern, $I(k_{||}, E)$, by changing the emission angle to the wave vector component parallel to the surface, $k_{||}$, using the relation (Fig. 1)

$$|k_{||}| = |k| \sin \theta = \frac{E_{ph}}{\hbar c} \sin \theta \quad (5)$$

where k is the wave vector for the emitted light, \hbar is Plank constant divided by 2π , and c is the velocity of light.

The SPP can be converted to a photon to emit light when it propagates on a periodic structure. The dispersion pattern transformed from the ARS pattern observed in the plasmonic crystal reveals the dispersion relation of SPP on the plasmonic crystal. The conversion between the photon and SPP mediated by plasmonic crystals must satisfy the following conditions in wave vector and energy,

$$k_p - k_{||} = G \quad (6a)$$

$$E_{SPP} = E_{ph} \quad (6b)$$

where k_p is the wave vector of the SPP, $k_{||}$ is the surface parallel component of the wave vector of light, and G is a reciprocal lattice vector of the surface structure. In eq.(6b), E_{SPP} and E_{ph} are energies of the SPP and light, respectively. The SPP is converted to photon at the crossing point between the dispersion curves of the SPP and dispersion line of photon emitted to the vacuum, i.e. $\omega = ck/\sin \theta$. Consequently the light is emitted along the dispersion curves of the SPP inside the light line as shown in Fig. 4(c).

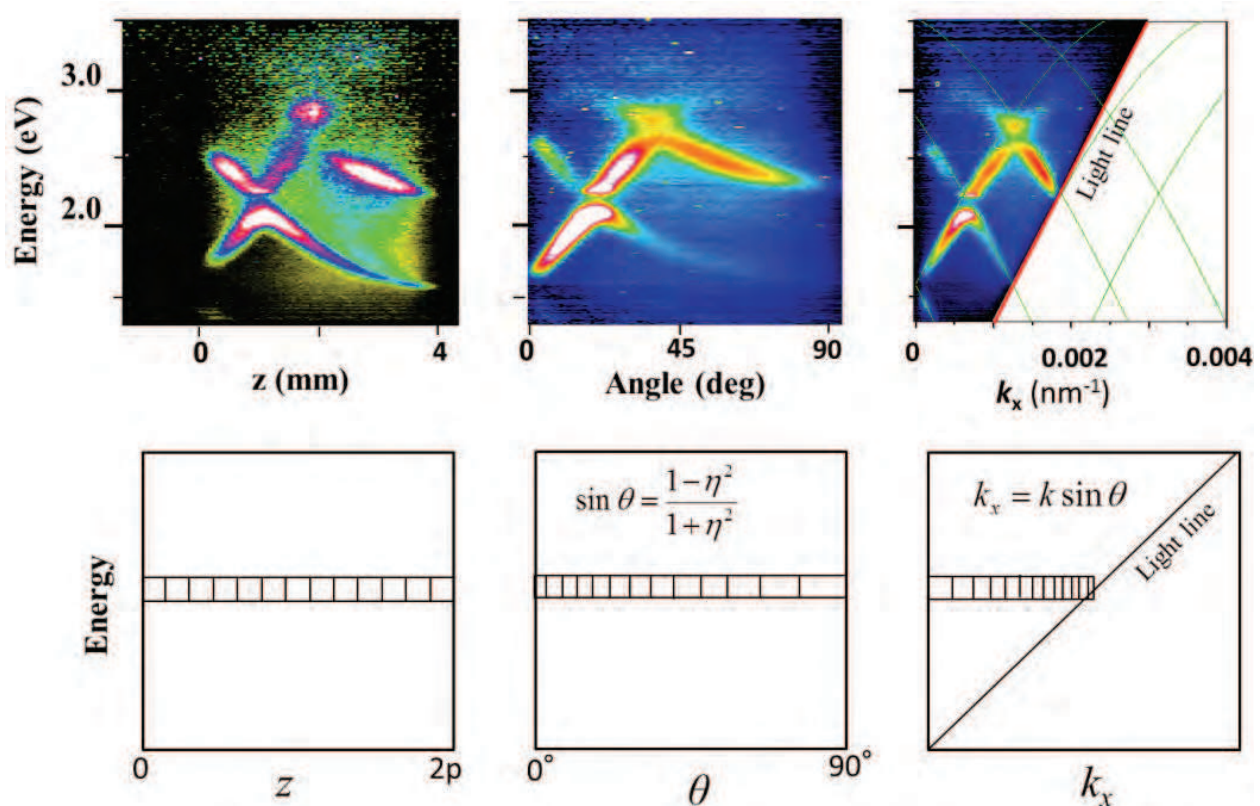


Fig. 4. (a) An original ARS pattern of an emission from a 1D-plasmonic crystal as a function of the hole position z , and (b) the ARS pattern transformed from (a) by changing the horizontal coordinate from z to θ . (c) Dispersion pattern transformed from (b) by changing to the wave vector component. (d) to (e) illustrate conversion of the intensity distribution from (a) to (c). Each square indicates an interval between neighboring data points corresponding to the original ones in (d).

Correction of spectrum and ARS pattern

1. Collection function of spectrum

The observed spectrum is modified from the true one due to the wavelength dependent efficiency of the detectors and other optical elements. The collection function of the total detection system is obtained as follows. A standard light source whose emission spectrum is known is set at the specimen position in TEM. We observe the emission spectrum by the detection system, and a collection function is obtained by dividing the true spectrum of the light source by the observed one. The transition radiation from an aluminum surface is frequently used as a standard light source, because it has a widely spreading spectrum over an optical range with a monotonously decreasing function inversely proportional to wavelength.

2. Conversion from wavelength to energy

Spectrum measured by the CCD detector consists of pixels with the same wavelength width. When the scale of the spectrum changes from wavelength to energy, the intensity should be collected by multiplying the following factor,

$$I(E) = I(\lambda) \left| \frac{d\lambda}{dE} \right| = I(\lambda) \frac{\lambda^2}{hc} = I(\lambda) \frac{hc}{E^2} \quad (7)$$

where h is Plank constant.

3. z - θ conversion

The mask has a hole of 0.5 mm in diameter and set in the X-Y stage. Solid angle subtended by the hole changes with emission angle, and is 0.1% of the total solid angle of hemisphere at $\theta=0^\circ$ and 0.4% at $\theta=90^\circ$. In the conversion of the ARS pattern from $I(z, E)$ to $I(\theta, E)$, the intensity should be collected for the angular dependence. From the relation

$$I(\theta, \varphi) \sin \theta d\theta d\varphi = I(y, z) dy dz \quad (8)$$

and eq. (4),

$$d\varphi = \frac{1}{1-\eta^2} \frac{1}{p} dy d\theta = -\frac{2}{1+\eta^2} d\eta = -\frac{1}{1+\eta^2} \frac{1}{p} dz, \quad (9)$$

we obtain

$$I(\theta) = I(z) p^2 (1+\eta^2)^2 \quad (10)$$

The term in the right side indicates the solid angle collection factor of the ARS pattern taken along the z axis.

4. θ - k_x conversion

In the conversion from the ARS pattern $I(\theta, E)$ to the dispersion pattern $I(k_x, E)$, the intensity should be collected according to the relation between θ and k_x . From the equations,

$$I(\theta, \varphi) \sin \theta d\theta d\varphi = I(k_x, k_y) dk_x dk_y \quad (11)$$

$$k_y = k \sin \theta \sin \varphi$$

and $k_x = k \sin \theta \cos \varphi$ and, the intensity should be multiplied by the following factor.

$$I(k_x) = I(\theta) \frac{1}{k^2 \cos \theta} \quad (12)$$

3. Transition radiation

Light emission caused by a high-energy electron passing through a medium are classified into several types from their characters, such as cathodoluminescence, Cherenkov radiation and transition radiation. Cherenkov radiation is generated when an electron moves in a transparent medium with a velocity higher than that of light, and transition radiation is generated when an electron passes across a boundary between two media with different dielectric constants. Characteristic features were observed in the emission spectra from thin

films of mica and silicon (Yamamoto et al., 1996, 2001a). In the case of mica films, the forward emission spectra showed a characteristic shape of Cherenkov radiation, whereas the backward emission spectra showed the intensity oscillation with respect to wavelength where the oscillation periodicity depends on accelerating voltage and film thickness. Similar oscillation was also observed in the emission spectra from silicon films. Such emissions are explained well from the theory derived by Ritchie and Eldridge (1962) and Pafomov and Frank (1967).

Here we describe the theory of transition radiation from a single boundary, because this radiation is always involved in the detected light from metal surfaces bombarded by electrons and must be considered in the analysis of the surface plasmon induced radiation. When an electron passes a boundary between two different media, transition radiation is generated from the boundary. Ginzburg and Frank (1946) first derived the formula of transition radiation for a single planar boundary. The formula for backward emission is written as

$$\frac{d^2 N}{d\lambda d\Omega} = \frac{\alpha \beta^2}{\pi \lambda} n_1 \sin^2 \theta_1 \cos^2 \theta_1 \times \left| \frac{(\varepsilon_2 - \varepsilon_1) (1 - \beta^2 \varepsilon_1 + \beta \sqrt{\varepsilon_2 - \varepsilon_1 \sin^2 \theta_1})}{(1 - \beta^2 \varepsilon_1 \cos^2 \theta_1) (1 + \beta \sqrt{\varepsilon_2 - \varepsilon_1 \sin^2 \theta_1}) (\varepsilon_2 \cos \theta_1 + \sqrt{\varepsilon_1 \varepsilon_2 - \varepsilon_1^2 \sin^2 \theta_1})} \right|^2 \quad (13)$$

where an electron passes through a planar boundary from medium 1 to medium 2 with a velocity v at normal incidence [Fig. 5(a)]. This formula gives a photon flux produced by a single electron in a wavelength range of $d\lambda$ and a solid angle of $d\Omega$, in which α is the fine structure constant ($\alpha = 1/137$), $\beta = v/c$ and $\varepsilon_1(\omega)$ and $\varepsilon_2(\omega)$ are the dielectric functions of the two media. The emission contains only the p -polarized component under the condition of normal incidence of the electron. Because the formula involves a factor β^2 in front, it is advantageous to use a higher accelerating voltage to observe transition radiation.

Spectra of the transition radiation is shown in Fig. 5(b) and (c) for normal incidence of an electron from a vacuum onto a silver surface calculated by using eq. (13) and the dielectric constant data of silver (Palik, 1985). Spectral shape changes with emission angle so as that the spectrum has a broad peak around 2.5-3 eV with a sharp dip at 3.8 eV (the bulk plasmon frequency of Ag), and the peak energy shifts to the lower energies with increasing emission angle.

Dependence of the transition radiation on emission angle is shown for several accelerating voltages in Fig. 5(d) for photon energy of 2.2 eV. The curve has a broad peak around 50° to 60°, and the peak position shifts to the lower angles with increasing accelerating voltage. Figures 5(e) and (f) show angular dependence for different photon energies at 200 kV. The peak energy is seen to shift to the lower angles with increasing photon energy.

In the case of a thin film surrounded by air, theoretical formula of the light emission intensity was derived by Ritchie and Eldridge (1962) and Pafomov and Frank (1967). Light emission from thin films of silver had been studied experimentally by many authors (Steinmann, 1961; Hattendorff, 1977), because the existence of the radiative surface plasmon mode was

predicted by Ferrell (1958) (the Ferrell mode) and the wavelength of the mode is in the optical region for silver. The emission corresponding to that mode was observed as a sharp peak at the bulk plasmon frequency in the backward emission spectra from a silver film. The observed dependence of spectral shape and intensity on accelerating voltage is in good agreement with the theory, when the specimen is a single-crystal film with a flat surface (Yamamoto et al., 2001a).

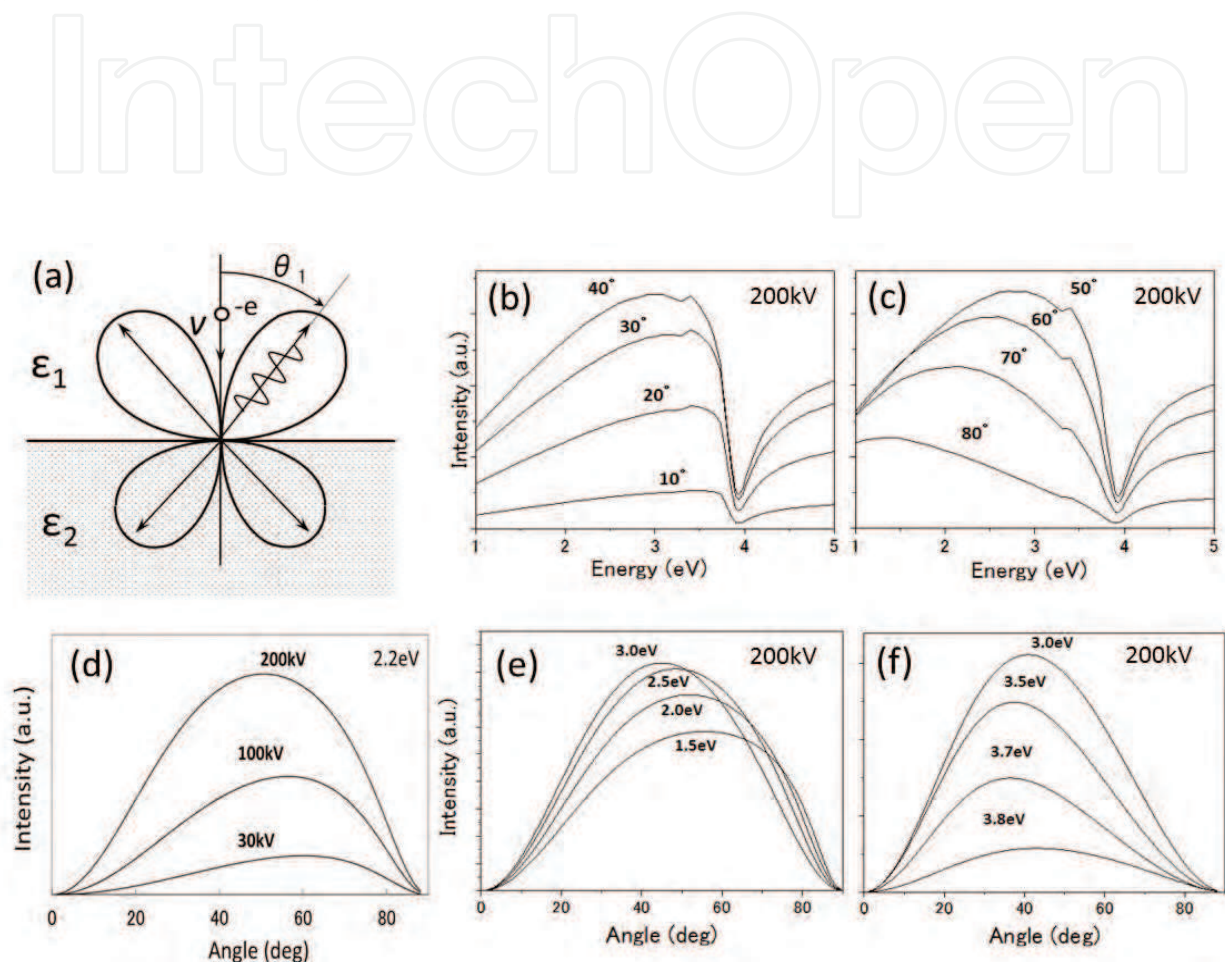


Fig. 5. (a) Diagram of angular distribution of transition radiation, (b), (c) angular dependence of TR spectrum from a silver surface, (d) accelerating voltage dependence of TR intensity, and (e), (f) photon energy dependence of angular distribution of TR.

4. Localized surface plasmon (LSP) in metal spheres

4.1 Single sphere - Mie mode

Light scattering by a metal sphere is well known and was treated by the classical electromagnetic theory (Mie, 1908). Electromagnetic oscillation modes are excited in a sphere by incidence of electrons and are transformed to photons to emit outside. In a non-retarded treatment, the energy of the sphere plasmons can be obtained by solving Poisson's equation, leading to the relation

$$\varepsilon(\omega_\ell) = -\frac{\ell+1}{\ell} \quad (14)$$

where ω_ℓ is the frequency of the localized surface plasmon modes associated with the orbital momentum number n and $\varepsilon(\omega)$ is the frequency-dependent dielectric function of the material of which the sphere is made up. A similar process is expected in the case of excitation of a metal sphere by an electron beam. Ferrell and Echenique (1985) derived a formula of electron energy loss probability for an electron passing near a dielectric sphere, and obtained the same condition for the resonance frequencies as eq. (14) calculated within a non-retarded treatment. Using the dielectric function of silver, the wavelengths obtained from this equation corresponding to the resonance frequencies are distributed in a narrow range that goes from 337 nm ($\ell = \infty$) to 354 nm ($\ell = 1$). However, the observed peaks appear at longer wavelengths, which cannot be explained by the above equation for the plasma oscillation frequencies in a sphere. Equation (14) determines the position of the loss peaks in the electron energy loss spectra calculated within a non-retarded treatment of the sphere electron interaction.

In the relativistic treatment involving the retardation effect, the probability of photon emission takes the following form (in atomic units) (Garcia de Abajo, 2002, 2010), when the electron trajectory does not pass through the sphere, as shown in Fig. 6(a),

$$\Gamma^{rad}(\omega) = \frac{1}{c\omega} \sum_{\ell=1}^{\infty} \sum_{m=-\ell}^{\ell} K_m^2\left(\frac{\omega b}{v\gamma}\right) \left[C_{\ell m}^M |t_\ell^M|^2 + C_{\ell m}^E |t_\ell^E|^2 \right] \quad (15)$$

where ω is the photon frequency, K_m is a modified Bessel function, v is the electron velocity, $\gamma = 1/\sqrt{1-\beta^2}$ is the Lorentz factor accounting for the retarded reduction of the sphere oscillation frequency as seen from the frame of the incoming electron, and b is the electron impact parameter with respect to the sphere center. The coefficients $C_{\ell m}^M$ and $C_{\ell m}^E$ inside the square brackets depend exclusively on β . t_ℓ^M and t_ℓ^E are scattering t -matrices for magnetic and electric modes in the Mie theory (Mie 1908). The electric modes are dominant for metallic spheres and for the electron velocities under consideration ($v/c=0.7$). Therefore, a given peak in an emission spectrum can be associated with a maximum of the scattering matrix element t_ℓ^E for a particular ℓ th-order mode. t_ℓ^E depends both on the sphere diameter D and on the dielectric function, but not on the electron velocity. This theory explains that the resonance energy of the Mie modes changes with diameter of sphere.

We have observed some anomalous features in the light emission from silver particles of 50~500 nm in diameter supported by a carbon thin film as shown in Fig. 6(a). Their spectra are characterized by multiple peaks whose relative intensities change with the position of the electron beam, which is focused on the target (Fig. 6(b)). Those peaks correspond to the Mie modes; the lowest energy peak indicated by red arrows in Fig. 6(b) corresponds to the dipole mode, and next one indicated by green arrows corresponds to the quadrupole mode. The observed peak energy shift with diameter of sphere is in good correspondence with theoretical one shown as colored back ground plot in Fig. 6(c).

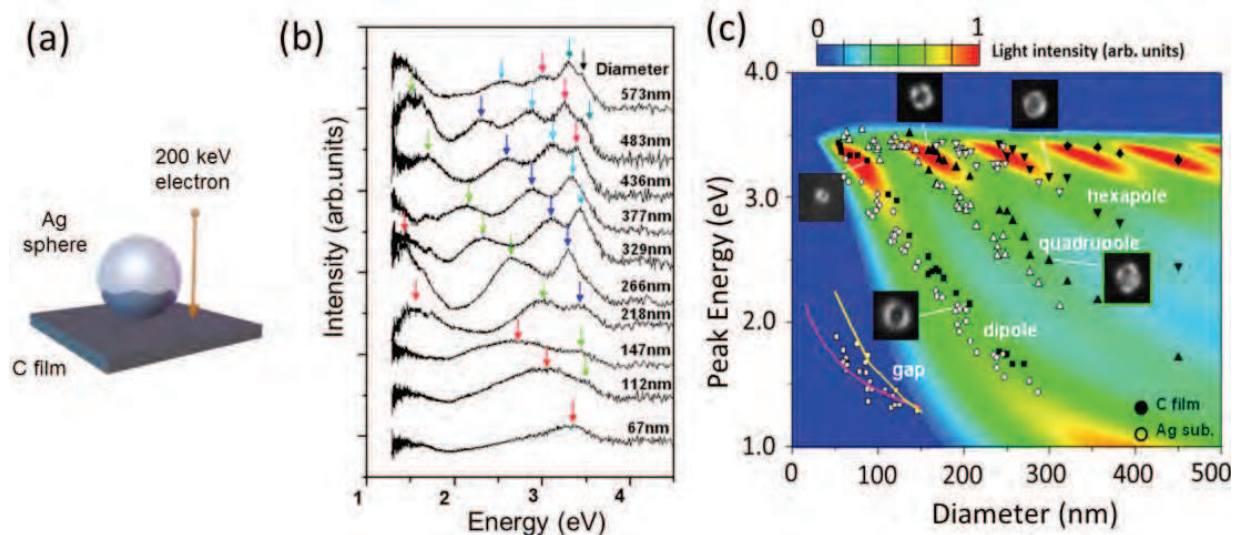


Fig. 6. (a) Excitation of Mie plasmons in silver particles excited by a grazing electron beam, and (b) emission spectra from silver particles with different diameters. (c) The size-dependent measured energies of Mie plasmons are represented and compared to the calculated cathodoluminescence intensity from self-standing particles under grazing incidence (background density plot). Open circles are observed peak energies from particles on a thick silver substrate (see ref. (Yamamoto et al., 2011)).

4.2 Metal sphere on substrate – Gap mode

Gap plasmons are observed at lower energies in the spectra from silver particles deposited on silver substrate when the beam spot is close to the center of the spheres, as shown in Fig. 7 (a). Angular dependence of the emission was measured under the arrangement of Fig. 7(a), which is shown in Fig. 7(b). Three peaks are identified from the beam-scan spectral images and photon maps taken at the emission energies; peak 1 is quadrupole Mie mode, peak 2 is dipole Mie mode and peak 3 corresponds to gap mode. The emission by the Mie mode is directed normal to the substrate surface, whereas the emission by the gap mode is directed over the higher angles. The angular distributions of those emissions are indicated in Fig. 7(c), where the emission intensities are plotted with open circles (dipole mode) and squares (gap mode).

The observed gap energies can be derived from the expression $\varepsilon(\omega) = -\varepsilon_d(1 + 2R/d)^{0.5}$, where ε and ε_d are the permittivities of silver and the material inside the gap, respectively, d is the gap distance, and R is the particle radius (Rendell and Scalapino, 1981). Red solid line in Fig. 6(c) is theoretical curve calculated by this expression. The yellow curve is another theoretical curve calculated for the emission from a dipole situated in the upper part of the spherical particle, opposite to the gap position, and oriented along the axis of symmetry (Yamamoto et al., 2011). The angular distribution is well explained by the emission from a dipole situated close to a planar silver surface and oriented perpendicular to it ($m = 0$ symmetry). The emission from the dipoles (solid curves in Fig. 7(c)) is calculated from the closed-form expressions (Novotny and Hecht, 2006).

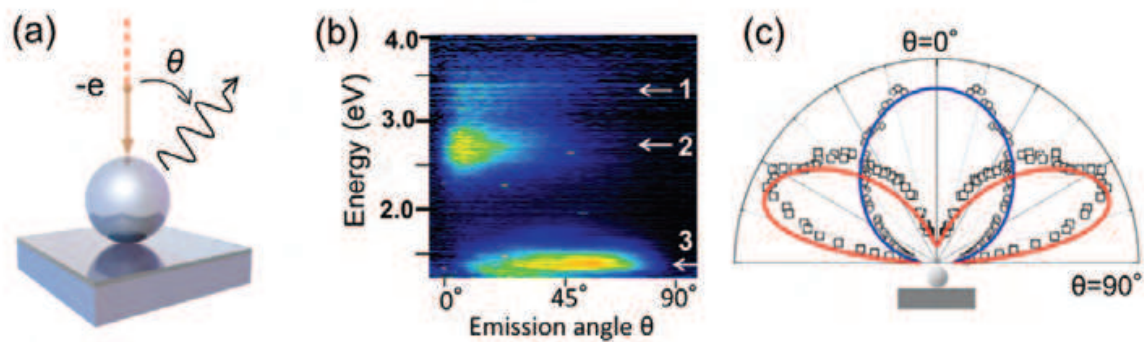


Fig. 7. (a) Arrangement for excitation of gap mode by an electron beam. (b) Angular dependence of the emission from dipole Mie (2) and gap (3) plasmons in supported spheres, and (c) schematic representation of the angular distribution. Theoretical curves are shown for gap plasmon (red) and dipole Mie plasmon (blue) (see Ref. (Yamamoto et al., 2011)).

5. SPP to light conversion at surface steps

5.1 Beam scan spectral image

A rectangular shaped terrace was fabricated on an InP substrate by electron beam lithography with a height of 100 nm and a width of 20 μm . Silver was deposited on the sample with a thickness of 200 nm by thermal evaporation in vacuum. Surface steps around the terrace were used for CL measurements and the experimental arrangement is illustrated in Fig. 8(a). Figure 8(b) shows a panchromatic photon map of the rectangular shaped terrace taken by the total photon intensity of the *p*-polarized light detected by the parabolic mirror. A fringe contrast appeared parallel to the surface steps when the monochromatic photon maps were observed at any photon energy (Yamamoto and Suzuki, 2008). Figure 8(c) clearly reveals a change in the fringe period with photon energy in the spectral image, which was taken by scanning the incident electron beam along the line A-B in Fig.8 (b). The direction of light detection was inclined by 43 $^\circ$ from the surface normal to the right side as depicted by the arrow in Fig. 8(b). The horizontal axis in the spectral image indicates the beam position, whereas the vertical axis indicates photon energy. The surface step was positioned at the center of the line, so the fringe patterns were discontinuous at the central vertical line in the spectral image.

In addition, the fringe contrast changed with the polarization direction. Herein *p*- (*s*-) polarization denotes the polarization direction parallel (perpendicular) to the plane determined by the surface normal and the emission direction of detected light. Figures 8(c) and (d) are the *p*- and *s*- polarized spectral images along the line A-B, respectively. A strong fringe contrast appeared in (c), but (d) had a negligible photon intensity and the contrast disappeared, indicating that the emission is strongly polarized in the *p* polarization direction. Figures 8(e) and (f) are *p*- and *s*- polarized spectral images along the line C-D with the same detection direction of light as that in (c) and (d), respectively. A fringe contrast, which had periods equal to those in neighboring terraces across the step, appeared in Fig. 8(e). However, the fringe contrast was asymmetrical about the step; the fringe started from the step with a bright contrast on the upper terrace [left side in Fig. 8(e)] and ended with a dark contrast on the lower terrace (right side). The phase of the fringe changed with photon energy. In Fig. 8(f), the fringe contrast disappeared on the terraces, but a bright contrast

localized at the step. The bright contrast can be attributed to the emission by a localized surface plasmon at the step edge (Dobrzynski and Maradudin, 1972). The emission had two broad peaks in the spectrum, and was strongly polarized perpendicular to the step as seen from Figs. 8(d) and (f).

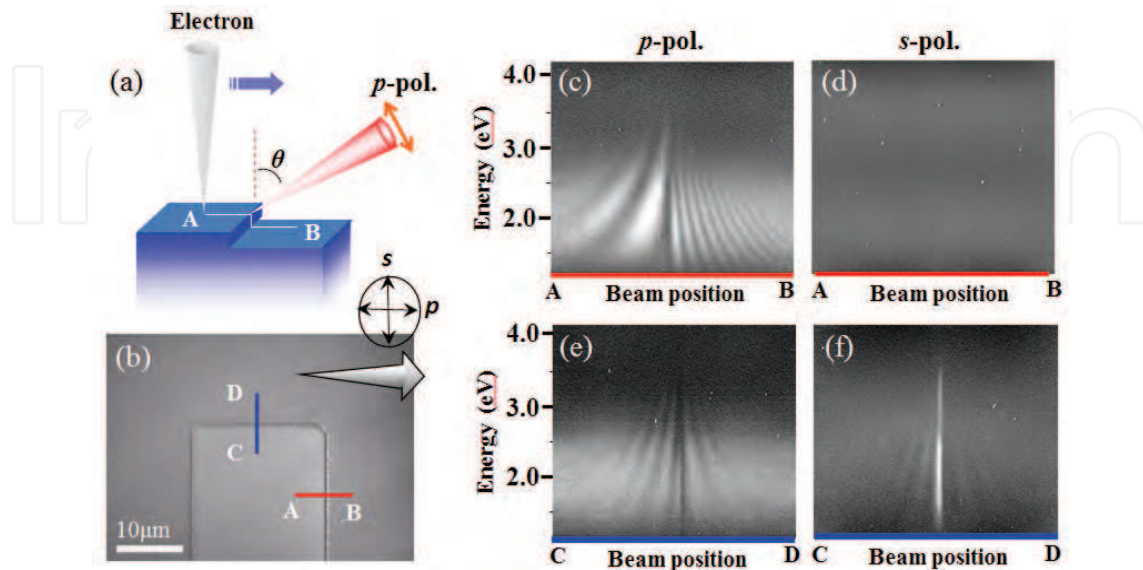


Fig. 8. (a) Panchromatic photon map of a rectangular shaped terrace. Spectral images taken by scanning the incident electron beam along the line A-B with (b) *p*-polarized and (c) *s*-polarized light emitted in the direction depicted by the arrow in (a). Spectral images taken along the line C-D with (d) *p*- and (e) *s*-polarized light. The light detection direction is tilted by 43° from the surface normal, and scanning distance along the lines is $8\mu\text{m}$. (Yamamoto and Suzuki, 2008)

The periods of the fringes in Fig. 8(c) differed on the two terraces; the period was shorter on the right terrace than on the left terrace. This property depended on the detection direction of light, but not on the type of the surface step. The fringe contrast can be explained by the interference between transition radiation (TR) and SPP induced radiation (SPPR) at the step as illustrated in Fig. 9 (Yamamoto and Suzuki, 2008). When the incident electron passed through the silver surface, transition radiation was generated due to the induced surface charge response. The transition radiation was *p*-polarized, and had a peculiar angular distribution. Simultaneously incident electrons excited SPPs with different energies. Each SPP propagated as a two-dimensional spherical wave from the incident point. When the SPP reached the surface step, it had a given probability of being decoupled into a photon radiating into free space.

The TR and the SPPR emitting in the direction of angle θ with a frequency ω are formulated as follows:

$$\psi_{TR} = A \frac{1}{R} \exp i(kR - \omega t) \quad (16)$$

$$\psi_{SPPR} = \int_{-\infty}^{\infty} E \cdot \frac{\exp(i k_p r)}{\sqrt{r}} S(\theta) \exp(-i \mathbf{k} \cdot \mathbf{r}) \frac{1}{R} \exp i(kR - \omega t) dy \quad , \quad (17)$$

where the amplitude A of the TR is expressed as a function of θ (Yamamoto and Suzuki, 2008) and the dielectric constants of silver (eq. (13)), and R is a distance from the incident point to the detector. In eq. (17), E is the excitation amplitude of SPP, S is the SPP to photon conversion efficiency expressed as a function of ω and θ , and k_p and k are wave numbers of the SPP and photon, respectively. Figure 9 depicts the Cartesian coordinates where the origin is set at the incident point. The integral in eq. (17) is taken along the step in the y direction where r is the position vector on the step, $r = (\pm x_0, y)$, where the + and - signs correspond to the cases in Fig. 9(a) and Fig. 9(b), respectively. In these equations, the polarization of each emission is selected to be parallel to the scattering plane formed by the surface normal and the emission direction (the p -polarization). The phase in the two-dimensional spherical wave of SPP in eq. (17) adds to the phase shift of light emitted from the step because it is expressed by:

$$k_p r = \omega_p \frac{r}{v_p} \omega \Delta t, \quad (18)$$

where v_p is the phase velocity of SPP and Δt is the time necessary for a SPP to propagate from the incident point to the step. Herein the frequency is conserved in the SPP to photon conversion process, i.e., $\omega_p = \omega$.

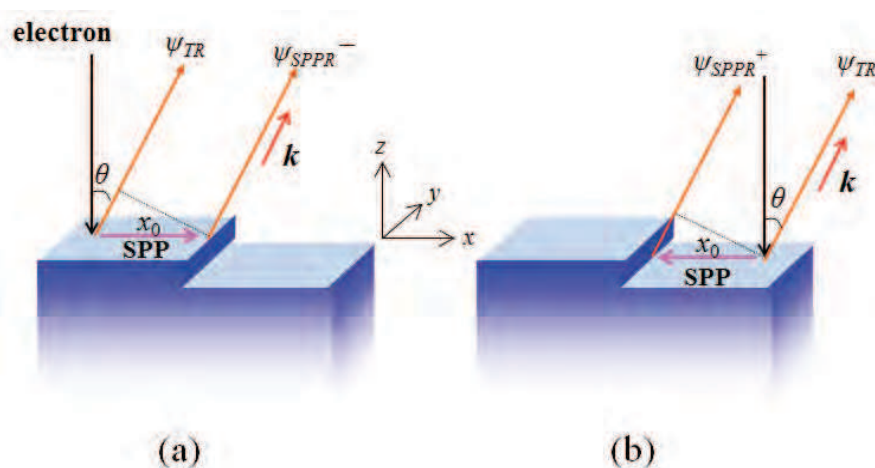


Fig. 9. Interference between transition radiation and SPP induced radiation at a surface step. (a) Electron beam is incident on the left side of the step, and (b) on the right side of the step.

Thus, the total emission intensity is given by the sum of the TR and SPP,

$$I_{Tot} = |\psi_{TR} + \psi_{SPP}|^2. \quad (19)$$

According to the analogy with the Fresnel zone in optics, it is anticipated that the main contribution in the integral in eq. (17) is due to part of the step inside the nearest zone defined by $x_0 < r < x_0 + \lambda_p/4$. The positive and negative contributions in the integral in eq. (17) are indicated by different colors in Fig. 10(a). The integrand in eq. (17) is indicated in Fig. 10(b) for $x_0 = \lambda$. It is noticed that only the central colored region can contribute to the integral. Therefore, when the incident point is sufficiently far from the step, i.e., $x_0 \gg \lambda_p$, only the SPPs propagating nearly normal to the step contribute to the SPPR.

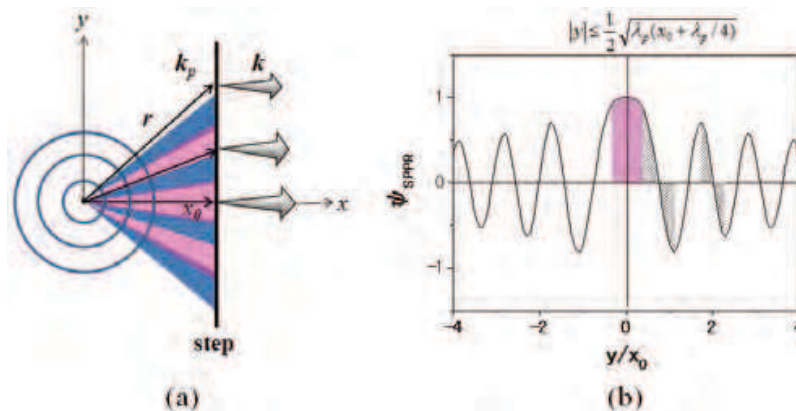


Fig. 10. (a) Geometry of the SPP to light conversion at a step. (b) The integrand in eq. (17) as a function of y for the case that $x_0 = \lambda_p$.

To confirm this, we observed beam-scan spectral images near the corner of the rectangular terrace with the detection angle of 43° as shown in Fig. 11(a). Spectral images (b) to (d) were taken along the lines in (a) far from the step by distances of (b) $1\mu\text{m}$, (c) $2\mu\text{m}$, and (d) $3\mu\text{m}$, respectively. Bright fringe contrasts are seen to appear in the spectral images which are due to the interference mentioned above. Their position can be derived from the fringe positions in Fig. 8(b). It is noticed that the bright fringe contrasts disappear in the left half of the images where the horizontal step is terminated at the center of the images. This fact clearly indicates that only the SPPs propagating nearly normal to the step contribute to the SPPR.

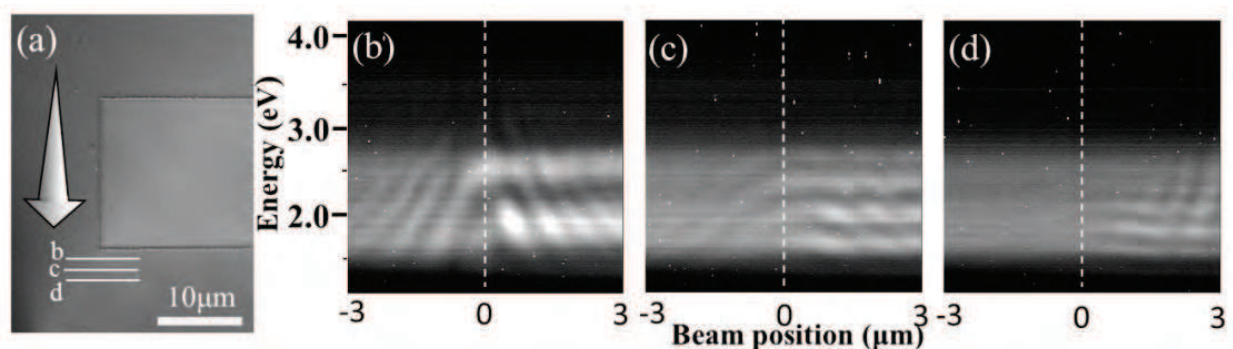


Fig. 11. (a) Panchromatic photon map of a rectangular shaped terrace. Spectral images (b) to (d) were taken by scanning the incident electron beam along the lines in (a) far from the step by distances of (b) $1\mu\text{m}$, (c) $2\mu\text{m}$, and (d) $3\mu\text{m}$, respectively.

Consequently, the condition that the two radiations emitted to the angle θ are cooperatively interfered is approximately expressed by the following equation:

$$k_p r - \mathbf{k} \cdot \mathbf{r} + \delta \cong k_p x_0 \mp k x_0 \sin \theta + \delta = 2n\pi \quad , \quad (20)$$

where $\mathbf{k} = (k \sin \theta, 0, k \cos \theta)$, and δ is a phase shift derived from the difference in phase among A , E , and S . The interference condition differs between the two cases shown in Figs. 9(a) and 9(b); the $-$ ($+$) sign corresponds to the case of Fig. 9(a) (Fig. 9(b)) where the incident point is located on the left (right) side of the step. The apparent wave numbers are defined from the observed fringe periods, λ^- and λ^+ , on the left and right side terraces, as follows:

$$K^+ = k_p + k \sin \theta = \frac{2\pi}{\Lambda^+}, \quad K^- = k_p - k \sin \theta = \frac{2\pi}{\Lambda^-}. \quad (21)$$

The interference condition of eq. (20) can be written using these parameters as:

$$K^\pm x_0 + \delta^\pm = 2n\pi. \quad (22)$$

It is possible to derive the wave number of SPP and the emission angle from the measured values of Λ^- and Λ^+ as:

$$k_p = \frac{1}{2}(K^+ + K^-), \quad \sin \theta = \frac{1}{2k}(K^+ - K^-). \quad (23)$$

In the case of Fig.8 (e) where $\mathbf{k} \cdot \mathbf{r} = 0$, then $K^+ = K^- = k_p$ and fringe contrast with the same period appears in the neighboring terraces. The period is equal to the wavelength of SPP.

Figure 12(a) shows the intensity profile along the section of the spectral image in Fig. 8(c) at an energy of 2.26 eV (550 nm in wavelength) where the origin of the horizontal axis is taken at the step. The bold solid lines depict the fitting curves calculated by eq. (19). Thus, the obtained fringe periods were $\Lambda^+ = 314 \pm 6$ nm and $\Lambda^- = 1410 \pm 30$ nm for the right and left side terraces, respectively. Using these values and eq. (23), the wavelength of SPP with an energy of 2.26 eV was 514 ± 15 nm, which is nearly equal to the expected value of 525 nm calculated for a SPP on a flat silver surface from the dielectric constants within an experimental error. The emission angle used to observe the spectral image was determined to be $\theta = 43 \pm 2^\circ$, which coincides with the angle estimated from the mask position. The initial phase of the fringes was $\delta^+ = -0.47\pi$ in the right side terrace, and $\delta^- = 1.05\pi$ for the left side terrace. This difference is due to the property of $S(\theta)$, which has a different value depending on how the SPP passes through the step, i.e., from the lower terrace to upper terrace or vice versa.

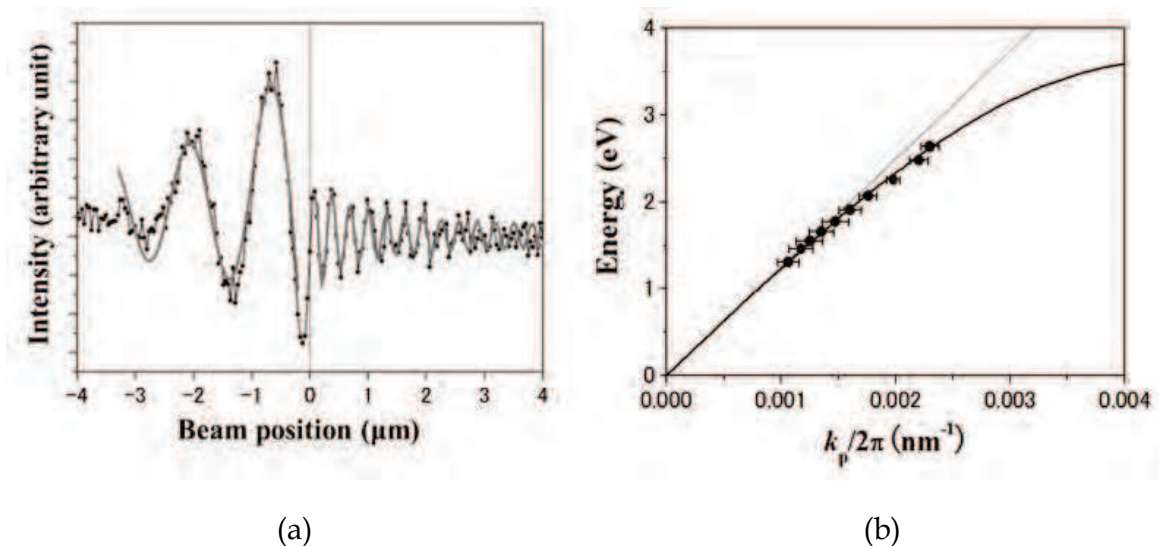


Fig. 12. (a) Intensity profile along the section of the spectral image in Fig. 8(b) at an energy of 2.26 eV (550 nm in wavelength). Bold solid lines are fitting curves for the data on both sides of the step. (b) Dispersion relation of SPP on a silver surface. Solid line is a dispersion curve calculated from the optical data. (Yamamoto and Suzuki, 2008)

The dispersion relation of SPP can be derived from the energy of photon and the wave number of the SPP calculated from the fringe periods at the same energy in the spectral image. Solid circles plotted in Fig. 12(b) show the result derived from the analysis of the interference fringes in Fig. 8(c). The solid line in Fig. 12 indicates the dispersion curve of the SPP propagating on a flat silver surface calculated from the optical data of silver (Palik, 1985). The plots agreed well with the solid line within the experimental error, indicating that the oxide layer on the silver surface does not affect the dispersion of SPP in our sample because the dispersion curve shifts to a lower energy if the oxide layer is thick.

The phase shift δ^\pm of the interference fringes is expressed by the phases in the transition radiation, excitation function and the SPP to photon conversion efficiency in eq. (16) and (17), and is written as follows,

$$\delta^\pm = \delta_E + \delta_S^\pm - \delta_{TR} . \quad (24)$$

The phase shift depends on the emission angle and photon energy, and can be obtained from the beam scan spectral images taken at several different emission angles as shown in Figs.13 (a)-(e). The asymmetry of the fringe contrast about the step becomes strong with the emission angle.

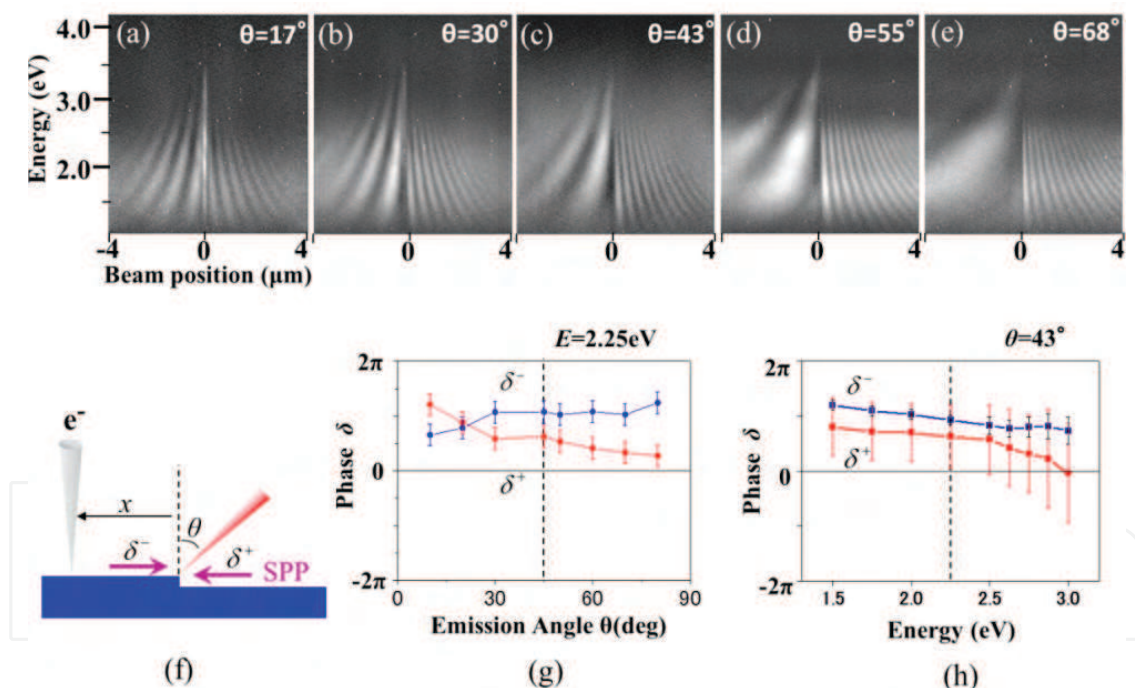


Fig. 13. The beam-scan spectral images taken at several emission angles, (a) 17° , (b) 30° , (c) 43° , (d) 55° , (e) 68° , respectively. (f) Schema of the phase shift in the SPP to light conversion at the step. (g) and (h) show dependence of the phase shift on emission angle and photon energy, respectively.

The two phase shifts δ^+ and δ^- are schematically depicted in Fig.13 (f). The phase shifts can be calculated from the analysis of these images using eq. (22). Thus we can obtain the dependence of the phase shift on emission angle and photon energy as shown in Fig.13 (g) and (h), respectively. Both of the phase shifts is close to π , and nearly constant in the wide

range of emission angle, except that they are crossing near $\theta=20^\circ$. The phase shifts are also seen to gradually decrease with photon energy (Fig. 13(h)).

Angular dependence of the SPPR was obtained by the angle-resolved measurement with an electron beam illuminated near a step. Figure 14(a) and (b) show angle-resolved spectral images taken with the electron beam fixed at a position (a) far from the step and (b) near the step. The emission pattern in Fig. 14(a) is mainly attributed to the transition radiation, whereas that in Fig. 14(b) is due to both transition radiation and SPP induced radiation at the step. Thus the intensity modulation results from interference between TR and SPPR as shown in Fig. 14(c), and can be expressed by eq. (19). Intensity profile of TR as a function of emission angle at an energy of 2.25 eV is plotted in Fig. 14(d). The theoretical curve of TR (blue line) shows good fit with the observed profile. Similarly the intensity modulation in Fig.14(b) is plotted in (e), and is fitted using eq.(19) with a proper parameter, a relative amplitude of SPPR with respect to TR. The angular distribution of the SPPR is derived as a red curve in Fig. 14(f). This distribution is rather broad compared to the theoretical one calculated by Sanchez-Gil (1998), in which the emission has sharp directionality at $\theta=70^\circ$. This could be attributed to the rounding of the step edge, which has a curvature of about 10 nm.

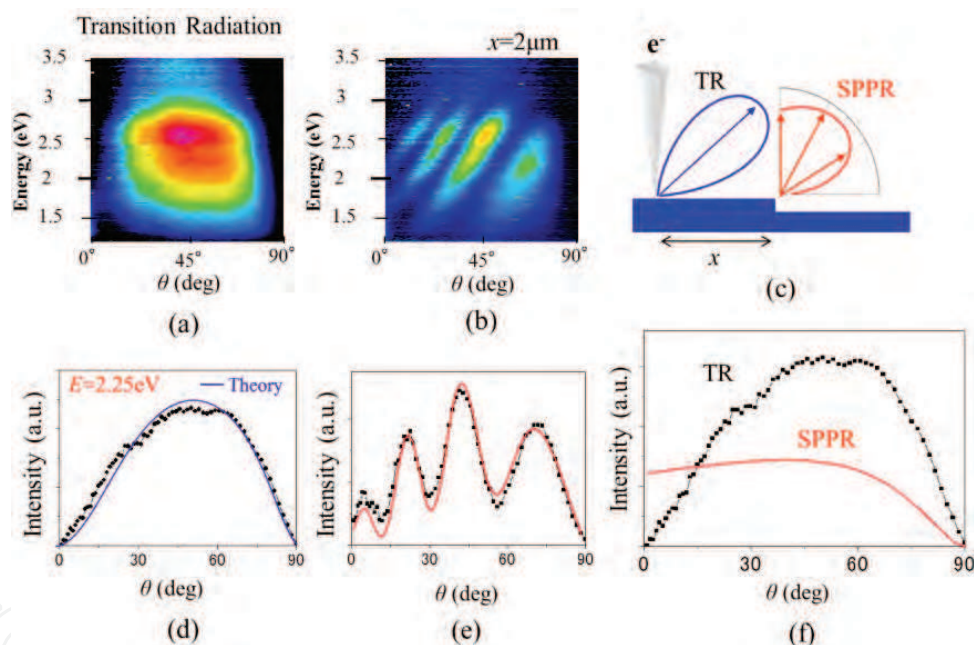


Fig. 14. Angle-resolved spectral images taken at a position (a) far from the step and (b) near the step ($x=2\mu\text{m}$). (c) shows interference between TR and SPPR. (d), (e) show intensity profiles in (a) and (b) at an energy of 2.25 eV. (f) shows an angular distribution of SPPR (red curve).

6. Plasmonic crystals

6.1 1D-plasmonic crystal

Angle-resolved measurements were performed with the sample in two different experimental arrangements shown in Fig. 15. In the first arrangement, shown in Fig. 15(a), the sample was placed such that the grating direction was parallel to the x axis. Figure 15(b) and (c) show angle-resolved spectral (ARS) patterns of p - and s -polarized emissions, respectively. During

the measurement the electron beam was scanned over an area of $5 \times 5 \mu\text{m}^2$. In the p -polarized ARS pattern of Fig. 15(b), a bright curved shape was observed, in which anti-crossing occurred at the crossing points of the curves. However, in the s -polarized ARS pattern of Fig. 15(c), the emission vanished and no contrast appeared. These results indicate that the detected emission is purely p -polarized in the setup of Fig. 15(a). Figure 15(e) and (f) were the ARS pattern measured in the setup shown in Fig. 15(d), in which the grating direction was perpendicular to the x axis. In the p -polarized ARS pattern of Fig. 15(e), spectra with a broad emission peak were observed over a large angular range. This emission is mainly due to the transition radiation (TR) emitted when an electron passes through a metal surface. The TR is also seen in Fig. 15(b) as a weak background. In the s -polarized ARS pattern of Fig. 15(f), several curved bright lines appear, which differ in shape from those in Fig. 15(b).

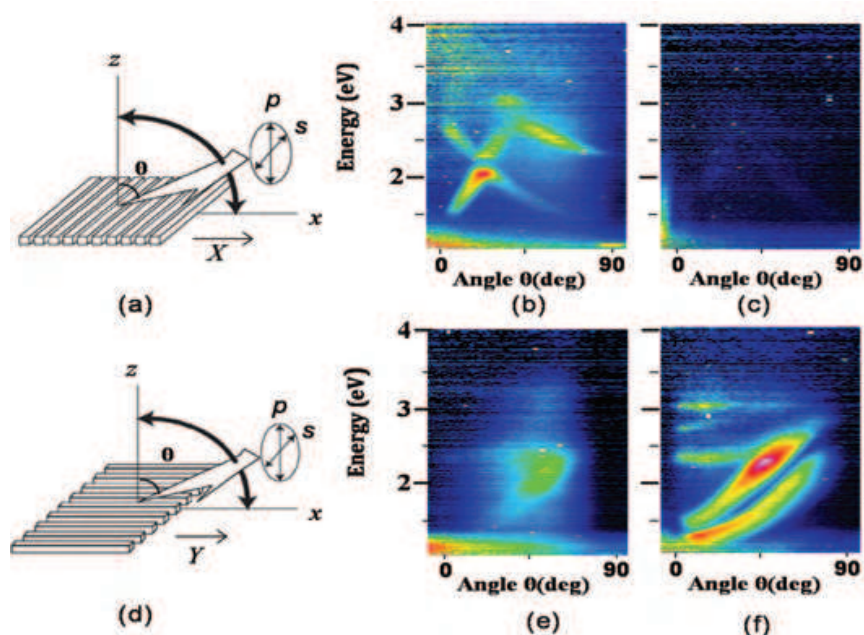


Fig. 15. (a) The arrangement for the angle-resolved measurements with the grating direction (the x direction) parallel to the parabolic axis of the mirror. (b, c) ARS patterns taken with the p - and s -polarized light, respectively, in the (a) arrangement. (d) The arrangement with a grating direction perpendicular to the parabolic axis. (e, f) ARS patterns taken with the p - and s -polarized light, respectively, arranged as in (d). (Suzuki and Yamamoto, 2009)

The ARS pattern is transformed into a dispersion pattern by changing the emission angle to the wave vector component parallel to the surface, $k_{||}$, using the relation of eq.(5). After the conversion of the abscissa, the ARS patterns in Fig. 15(b) and (f) are transformed into the dispersion patterns in Fig. 16(a) and (b), respectively.

A surface plasmon polariton on a periodic structure is similar to a Bloch wave. When the wave vector is far from the Brillouin zone boundary, the SPP is plane wave-like, whereas it becomes a standing wave when the wave vector is at the Brillouin zone boundary. Solid lines in Figs. 16(a) and (b) indicate dispersion curves of SPP in the 1D-plasmonic crystal along the grating direction (the X direction in Fig. 15(a)) and the perpendicular direction, respectively. These curves are made by successive shift of the dispersion curve of SPP in a flat surface by the reciprocal lattice vector G (the empty lattice approximation), though energy gaps open up at the Brillouin zone boundaries in the real plasmonic crystal. As mentioned in section 2, the

dispersion curves of SPP are revealed inside the light line in the dispersion pattern. Similar result was obtained by Heitmann (1977). The SPP dispersion curves are seen to fit with the observed contrasts in Fig.16. The splitting of the bright line contrasts in Fig. 16(b) is due to dissociation of the degenerated SPP modes along the Brillouin zone boundary, corresponding to the two SPP standing wave modes (Suzuki and Yamamoto, 2009).

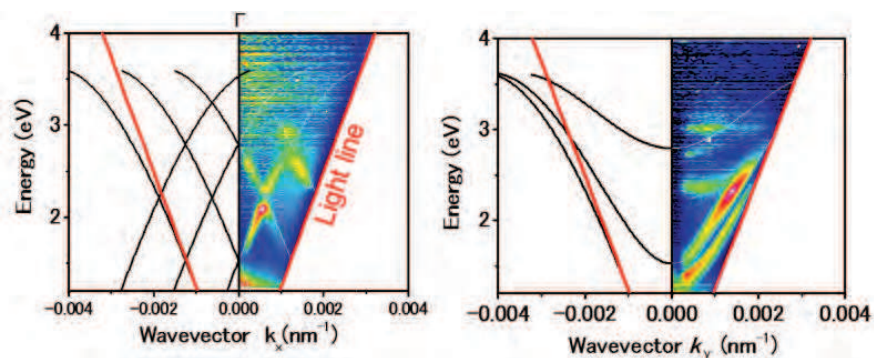


Fig. 16. (a, b) Dispersion patterns transformed from Fig.2 (b) and (f), respectively. (Suzuki and Yamamoto, 2009)

Emission spectra were successively measured by scanning the electron beam along the x direction in the experimental arrangement of Fig. 14(a), with the mask fixed at the position indicated by an arrow ($\theta = 20^\circ$) in Fig. 17 (a). Figure 17(b) shows a spectral image created by aligning the observed spectra with respect to the electron beam position, where the vertical axis indicates photon energy. This is a typical example of the beam-scan spectral image of the 1D plasmonic crystal. This image reveals spatial distribution of the SPP standing waves of the band edge at the Brillouin zone boundary. The SPP standing wave at $E=2.28\text{eV}$ is a symmetry mode (ω_+ mode) having an antinode at the center of the terrace, and that at $E=2.09\text{eV}$ is an asymmetry mode (ω_- mode) having a node at the center. The charge distributions of the two modes are illustrated in Fig. 17(c).

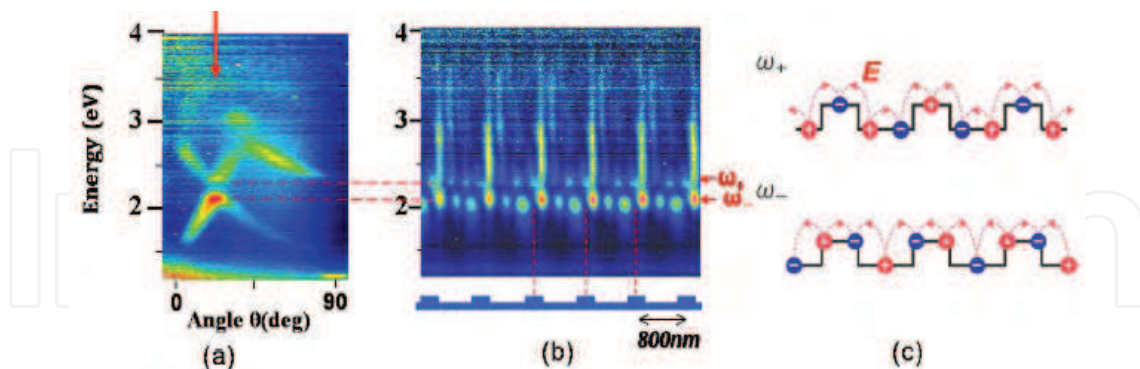


Fig. 17. (a) The ARS pattern in Fig. 14 (b). (b) A beam-scan spectral image taken with a scanning electron beam across the grating. (c) Illustration of charge distribution and the electric field of the two SPP standing waves. (Suzuki and Yamamoto, 2009)

6.2 2D-plasmonic crystal

Figure 18(a) shows the SEM image of an array of cylindrical holes on an InP substrate created by electron-beam lithography. A square lattice in the array has a periodicity of 600 nm, and the holes have a diameter and depth of 300 nm and 100 nm, respectively. A 200-nm

thick silver layer is evaporated onto the substrate by thermal evaporation in a vacuum. Figure 18(b) illustrates the reciprocal lattice of this 2-D plasmonic crystal structure. Figures 18(c)-(f) show the dispersion patterns along the Γ -X direction for (c) p -polarized and (d) s -polarized emissions, and along the Γ -M direction for (e) p -polarized and (f) s -polarized emissions. These patterns were made by folding a right-half pattern to the left.

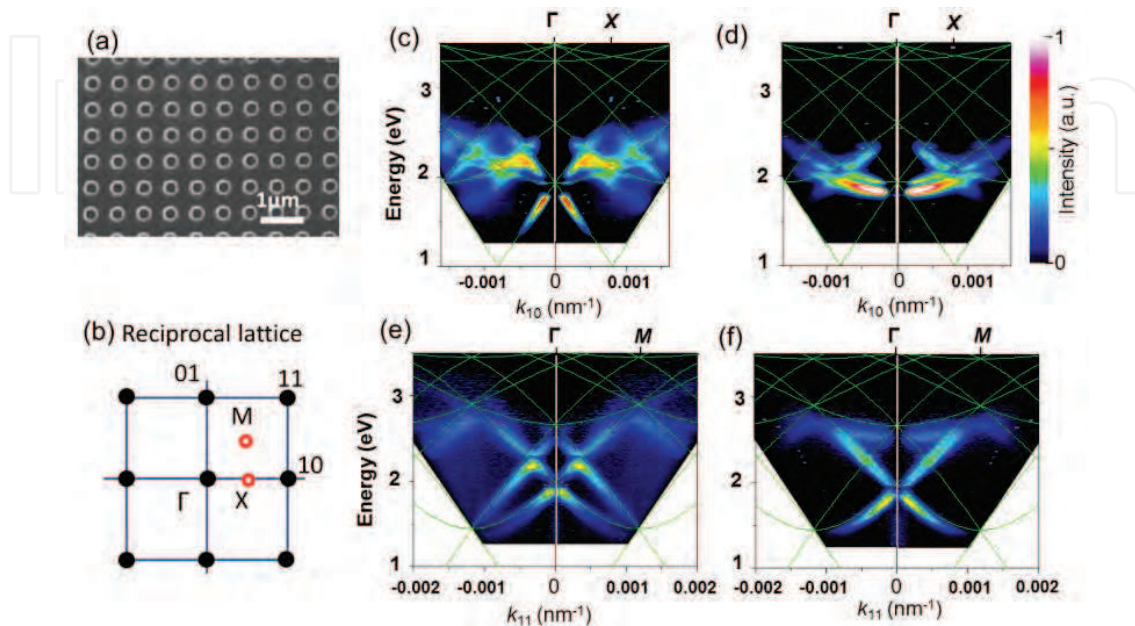


Fig. 18. Dispersion patterns of 2-D plasmonic crystal. (a) SEM image of a specimen, (b) a reciprocal lattice. (c) and (d) show dispersion patterns along the Γ -X direction for p -polarized and s -polarized emissions, and (e) and (f) are those along the Γ -M direction. (Takeuchi and Yamamoto, 2011)

In the dispersion patterns, bright curved contrasts, which appear along the SPP dispersion curves (green lines), depend on the polarization direction of the emitted light. In the dispersion pattern in the Γ -X direction, split line contrasts along the horizontal dispersion curve appear in the s -polarization (Fig. 18(d)), but disappear in the p -polarization (Fig. 18(c)). However, the other line contrasts are elongated from nearly the same energy position (~ 1.9 eV) at the Γ point. These contrasts appear in the p -polarization (Fig. 18(c)), but disappear in the s -polarization. The dispersion patterns in the Γ -M direction exhibit a similar dependence on the polarization direction; a gap occurs at the closing point of the dispersion curves in the p -polarization (Fig. 18(e)), but not in the s -polarization (Fig. 18(f)). The dependence of these contrasts on polarization is explained by considering the SPP modes associated with the photon emission under the condition of eq. (6) (Takeuchi and Yamamoto, 2011).

Figure 19(a) shows an ARS pattern of p -polarized emission near the surface normal direction acquired by tilting the specimen in the $[1,0]$ direction with respect to the incident beam direction and Fig. 19(b) illustrates a schematic diagram of the dispersion curves along the Γ -X direction. The four dispersion lines gather at the Γ point. The line contrast of the highest energy mode appears only in p -polarization, although it disappears at the Γ point. Therefore, this mode should correspond to the A mode, which does not emit light, due to the symmetrical charge distribution around the hole. The E mode at the Γ point is doubly degenerated, and the lowest energy mode can correspond to this mode. Those modes can be identified from pattern in the photon maps.

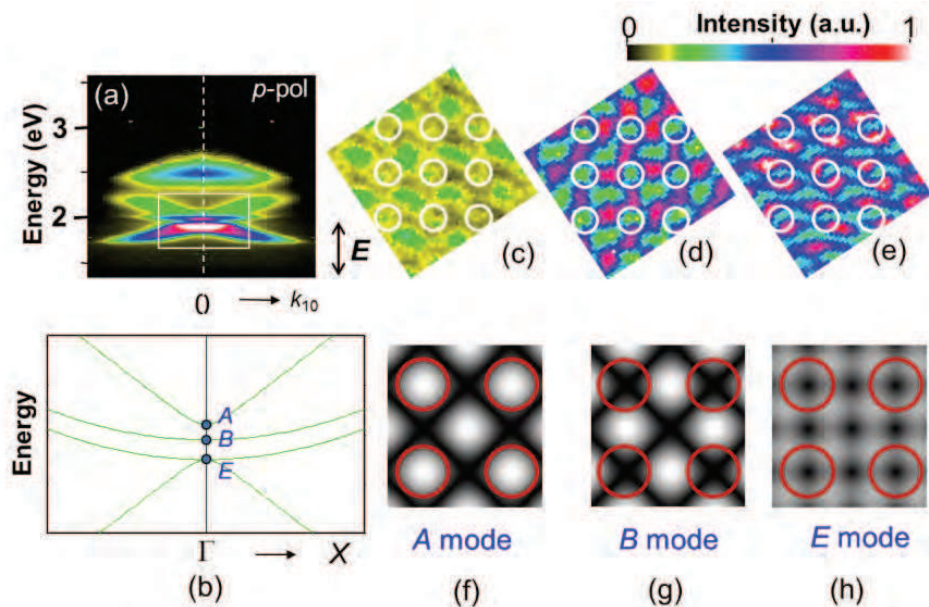


Fig. 19. ARS pattern near the Γ point taken by p -polarized emission. (b) Schematic diagram of the dispersion curves along the Γ - X direction. Photon maps taken by the p -polarized emission at peak energies of (c) 2.067 eV, (d) 2.002 eV, (e) 1.944 eV. (i)–(k) show patterns of the time-averaged field strength associated with the SPP modes at the Γ point. Red circles indicate holes. (Takeuchi and Yamamoto, 2011)

Figures 19(c)–(e) are photon maps taken with light emitted near the surface normal direction at the peak energies of the Γ point for the p -polarization where the white circles denote hole positions. It has been reported that a photon map acquired via the cathodoluminescence technique under the proper conditions mimics the field distribution of standing SPP waves or the local electromagnetic density of states (EMLDOS) (Suzuki and Yamamoto, 2009; García de Abajo and Kociak, 2008; Kuttge et al., 2009; Boudarham et al. 2010). Figures 19(f)–(h) show patterns of the time-averaged field strength associated with the SPP modes at the Γ point, i.e., the square modulus of the field amplitude. There is a clear correlation between the photon maps and calculated patterns. The SPP to photon conversion mechanism in the plasmonic crystal can be explained by the idea that a collective oscillation of an induced surface charge of the SPP forms an oscillating electric dipole around the edge of the hole to emit light (Takeuchi and Yamamoto 2011).

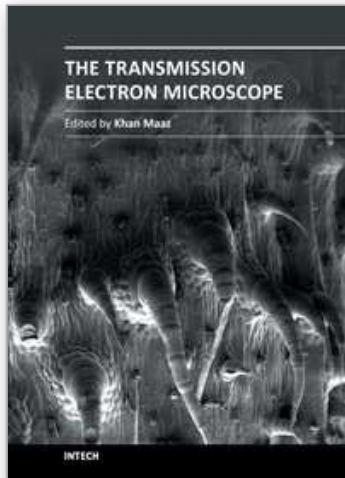
7. Conclusion

High energy electrons can excite surface plasmon polaritons (SPPs) in metal particles and nanostructures on metal surfaces. The excited SPPs are converted to photons via surface morphologies. The emitted light induced by incident electrons through SPP excitation inside a TEM/STEM can be detected by the TEM/STEM-CL system. The characteristic properties of CL in SPP excitation on metal surfaces are as follows: (1) it can generate an SPP point source at any position on the sample surface, regardless of the shape of the surface, (2) all the SPP modes with continuous energies can be excited, and (3) the excited SPP propagates in all directions from the electron incident point as a 2-dimensional spherical wave. The electron beam can be focused to a nanometer-sized spot, thus high spatial resolution can be achieved for CL imaging. By selecting the direction of the SPP-induced light in the angle-resolved measurement, we can investigate an individual SPP mode with a specific energy

and propagation direction. Then the dispersion relation of the SPP in the specific direction was derived from the angle-resolved spectrum. The emission intensity distribution in the spectral image taken with scanning electron beam at the selected detection angle revealed the SPP standing wave patterns at the band edge energies. These results indicate that CL is a useful technique for investigating the properties of SPP in plasmonic crystals and related structures such as cavity and wave guide composed of metallic materials.

8. References

- Brongersma, M. L. and Kik, P.G., ed., 2007, "Surface Plasmon Nanophotonics, Springer Series in Optical Sciences," Vol.131.
- Boudarham, G., Feth, N., Myroshnychenko, V., Linden, S., García de Abajo, F. J., Wegener, M., and Kociak, M., *Phys. Rev. Lett.* 105, 255501 (2010)
- Catchpole, K.R. and Polman A., 2008, *Opt. Express*, 16, 21793.
- Dobrzynski, L. and Maradudin, A.A., 1972, *Phys. Rev. B* 6, 3810.
- Ferrell, R.A., 1958, *Phys. Rev.* 111, 1214.
- Ferrell, T.L., Echenique, P.M., *Phys. Rev. Lett.* 1985, 55, 1526.
- García de Abajo, F. J., Howie, A. *Phys. Rev. B* 2002, 65, 115418.
- García de Abajo, F. J., *Rev. Mod. Phys.* 2010, 82, 209–275.
- García de Abajo, F. J., and Kociak, M., *Phys. Rev. Lett.* 100, 106804 (2008).
- Ginzburg V.L., Frank I.M., 1946, *JETP (USSR)* 16: 15; 1946, *J. Phys.* 9: 353.
- Heitmann, D., 1977, *J. Phys. C*, 10, 397.
- Hattendorff, H.D., 1977, *Phys. Status Solidi A* 42,489.
- Homola, J., *Chem. Rev.* 108 (2008) 462-493.
- Kuttge, M., Vesseur, E. J. R., Koenderink, A. F., Lezec, H. j., Atwater, H, A, García de Abajo, F. J., and Polman A., 2009, *Phys. Rev. B* 79, 113405.
- Maier, S.A., 2007, "Plasmonics: Fundamentals and Applications", Springer.
- Mie, G., 1908, *Ann. Phys. (Leipzig)*, 25, 377–445.
- Novotny, L. and Hecht, B., 2006, *Principles of Nano-Optics*; Cambridge University Press: New York.
- Pafomov, V.E. and Frank I.M., 1967, *Sov. J. Nucl. Phys.* 5: 448.
- Palik, E.D. 1985, *Handbook of Optical Constants of Solids*, (Academic Press, New York).
- Raether, H., 1988, "Surface plasmons on smooth and rough surfaces and on gratings" (Springer-Verlag, Berlin).
- Rendell, R. W. and Scalapino, D. J., 1981, *Phys. Rev. B*, 24, 3276–3294.
- Ritchie, R.H, Eldridge, H.B., 1962, *Phys. Rev.* 126, 1935-1947.
- Sanchez-Gil, J.A., 1998, *Appl. Phys. Lett.* 73, 3509 .
- Steinmann, W., 1961, *Phys. Rev. Lett.* 5, 470.
- Suzuki, T and Yamamoto, N., 2009, *Opt. Express*, 17, 23664-23671.
- Takeuchi, K., and Yamamoto, N., 2011, *Opt. Express*, 19, 12365-12374.
- Yamamoto, N., Sugiyama, H. and Toda, A. 1996, *Proc.Roy.Soc.London A*, 452, 2279-2301.
- Yamamoto, N., Araya, K., Toda, A. and Sugiyama, H., 2001a, *Surf. Interface Anal.* 31, 79-86.
- Yamamoto, N., Araya, K. and García de Abajo, F. J., 2001b, *Phys. Rev.B* 64, 205419.
- Yamamoto, N., Nakano, M. and Suzuki, T., 2006, *Surf. Interface Anal.* 38, 1725-1730.
- Yamamoto, N. and Suzuki, T., 2008, *Appl. Phys. Lett.* 93, 093114.
- Yamamoto, N., "Handbook of Nanophysics ; Nanoelectronics and Nanophotonics", (2010) Taylor&Francis Pub. (CRC Press), Ch.21, p1-25.
- Yamamoto, N., S. Ohtani, S., and García de Abajo, F.J., 2011, *Nano Lett.*, 11, 91–95.



The Transmission Electron Microscope

Edited by Dr. Khan Maaz

ISBN 978-953-51-0450-6

Hard cover, 392 pages

Publisher InTech

Published online 04, April, 2012

Published in print edition April, 2012

The book "The Transmission Electron Microscope" contains a collection of research articles submitted by engineers and scientists to present an overview of different aspects of TEM from the basic mechanisms and diagnosis to the latest advancements in the field. The book presents descriptions of electron microscopy, models for improved sample sizing and handling, new methods of image projection, and experimental methodologies for nanomaterials studies. The selection of chapters focuses on transmission electron microscopy used in material characterization, with special emphasis on both the theoretical and experimental aspect of modern electron microscopy techniques. I believe that a broad range of readers, such as students, scientists and engineers will benefit from this book.

How to reference

In order to correctly reference this scholarly work, feel free to copy and paste the following:

Naoki Yamamoto (2012). Cathodoluminescence of Surface Plasmon Induced Light Emission, The Transmission Electron Microscope, Dr. Khan Maaz (Ed.), ISBN: 978-953-51-0450-6, InTech, Available from: <http://www.intechopen.com/books/the-transmission-electron-microscope/cathodoluminescence-of-surface-plasmon-induced-light-emission>

INTECH
open science | open minds

InTech Europe

University Campus STeP Ri
Slavka Krautzeka 83/A
51000 Rijeka, Croatia
Phone: +385 (51) 770 447
Fax: +385 (51) 686 166
www.intechopen.com

InTech China

Unit 405, Office Block, Hotel Equatorial Shanghai
No.65, Yan An Road (West), Shanghai, 200040, China
中国上海市延安西路65号上海国际贵都大饭店办公楼405单元
Phone: +86-21-62489820
Fax: +86-21-62489821

© 2012 The Author(s). Licensee IntechOpen. This is an open access article distributed under the terms of the [Creative Commons Attribution 3.0 License](#), which permits unrestricted use, distribution, and reproduction in any medium, provided the original work is properly cited.

IntechOpen

IntechOpen